Computers in Biology and Medicine 106 (2019) 114–125

Contents lists available at ScienceDirect

Computers in Biology and Medicine

journal homepage: www.elsevier.com/locate/compbiomed

Pathophysiological mapping of tumor habitats in the breast in DCE-MRI using molecular texture descriptor

Otilio Paulo da Silva Neto[a,b,*], José Denes Lima Araújo[b], Ana Gabriela Caldas Oliveira[b], Mara Cutrim[b], Aristófanes Corrêa Silva[b], Anselmo Cardoso Paiva[b], Marcelo Gattass[c]

[a] Federal Institute of Piauí, Teresina, Piauí, Brazil
[b] Federal University of Maranhão, Brazil
[c] Pontifical Catholic University of Rio de Janeiro, Rio de Janeiro, Brazil

ARTICLE INFO

Keywords:
Breast cancer
Automated breast detection
Molecular texture descriptor
Pathophysiological mapping
Magnetic resonance imaging

ABSTRACT

Background: We propose a computational methodology capable of detecting and analyzing breast tumor habitats in images acquired by magnetic resonance imaging with dynamic contrast enhancement (DCE-MRI), based on the pathophysiological behavior of the contrast agent (CA).
Methods: The proposed methodology comprises three steps. In summary, the first step is the acquisition of images from the Quantitative Imaging Network Breast. In the second step, the segmentation of the breasts is performed to remove the background, noise, and other unwanted objects from the image. In the third step, the generation of habitats is performed by applying two techniques: the molecular texture descriptor (MTD) that highlights the CA regions in the breast, and pathophysiological texture mapping (MPT), which generates tumor habitats based on the behavior of the CA. The combined use of these two techniques allows the automatic detection of tumors in the breast and analysis of each separate habitat with respect to their malignancy type.
Results: The results found in this study were promising, with 100% of breast tumors being identified. The segmentation results exhibited an accuracy of 99.95%, sensitivity of 71.07%, specificity of 99.98%, and volumetric similarity of 77.75%. Moreover, we were able to classify the malignancy of the tumors, with 6 classified as malignant type III (WashOut) and 14 as malignant type II (Plateau), for a total of 20 cases.
Conclusion: We proposed a method for the automatic detection of tumors in the breast in DCE-MRI and performed the pathophysiological mapping of tumor habitats by analyzing the behavior of the CA, combining MTD and MPT, which allowed the mapping of internal tumor habitats.

1. Introduction

In recent years, advances in targeted therapy for cancer treatment have significantly aided the search for new therapies to monitor tumor changes resulting from the therapy used. Therapeutic monitoring studies reveal that late detection of alterations in underlying tumor characteristics, such as vascularization, vascular permeability, cellularity, metabolism, and biochemistry have severe implications on the treatment of cancer patients [1–4]. Thus, imaging modalities that can quantify tumor functions are becoming increasingly crucial for the evaluation and prediction of therapeutic response [1,2].

Magnetic resonance imaging with dynamic contrast enhancement (DCE-MRI) is a minimally invasive imaging method that measures changes in microvascular tissue properties. This method has been widely used in research and clinical trial configurations in the preliminary phase, to assess the therapeutic response of the tumor [2,4–6].

Globally, recent studies have provided recommendations on data acquisition and analysis in DCE-MRI, so as to evaluate the response of the tumor to therapy. In Refs. [1,7–9], the authors claim that a quantitative approach to DCE-MRI analysis using pharmacokinetic models allows the extraction and mapping of quantitative parameters of tumor biology *in vivo*. These parameters are generally variants of a contrast agent (CA) applied to the patient. This reaction contrasts with the volume of the interstitial space (extracellular and extravascular), enhancing the most vascularized regions of the breast [9,10].

A new approach in the analysis of tumors in DCE-MRI is the characterization of their regions based on the behavior of the CA, and a more complete analysis can be performed in these contrasted regions,

* Corresponding author. Federal Institute of Piauí, Teresina, Piauí, Brazil.
E-mail addresses: otilio.paulo@ifpi.edu.br (O.P. da Silva Neto), josedenes@nca.ufma.br (J.D.L. Araújo), gabriela.caldas1971@gmail.com (A.G. Caldas Oliveira), mara.cutrim@dugaich.com (M. Cutrim), ari@dee.ufma.br (A.C. Silva), anselmo@dee.ufma.br (A.C. Paiva), mgattass@inf.puc-rio.br (M. Gattass).

https://doi.org/10.1016/j.compbiomed.2019.01.017
Received 27 August 2018; Received in revised form 16 January 2019; Accepted 19 January 2019

giving the expert physician a more accurate diagnosis. However, the use of this approach is not enough to ensure an accurate analysis. Robust and coordinated tuning of its characteristics is required, as well as innovative techniques that have attracted the attention of many research groups, both in industry and academia [1,6].

The literature presents several methodologies to solve the problem of characterizing tumor regions. Methods for the detection of habitats based on the response to the treatment of cancerous tumors are widely used [4,6,9,11]. Although these methods have been well established, much remains to be done, such as the detection of tumor candidate regions and the individual analysis of habitats. These challenges motivate research on new techniques for monitoring the treatment of patients suffering from breast cancer.

In recent decades, many tumor analysis techniques have been developed and applied in several studies [4,5,12]. In the context of DCE-MRI analysis, techniques based on tumor habitats have been successfully applied. The analysis of tumor habitats is relevant and applies to the proposed problem, because the results obtained by these techniques can be improved. In addition, the temporal analysis of the tumoral habitats in the breast in DCE-MRI aims to improve the diagnosis and treatment of patients suffering from breast cancer, which is a well-studied problem in the literature [1,4].

In this work, we propose the analysis of cancerous tumor habitats in DCE-MRI. The novel aspects of the work are the automatic segmentation of tumors in the breast and the individual analysis of their habitats based on the pathophysiological behavior of the CA of the DCE-MRI in treatment, which allow the evaluation and prediction of the therapeutic response in cancer patients. Additionally, we propose a new molecular texture descriptor (MTD), based on chemical laws, and the pathophysiological texture mapping in DCE-MRI (MPT), which uses the behavior of the CA within the breast to map tumor regions. These act in concert to automatically detect tumor regions in the breast in DCE-MRI, allowing the generation of the pathophysiological mapping of tumor habitats and enabling their individual analysis.

The remainder of this paper is structured as follows: Section 2 presents the materials and methods used in this study, emphasizing the MTD, which is based on the laws of chemistry, and the MPT, which uses the behavior of the CA within the breast to map the tumor habitats. As previously stated, these act together to automatically detect the tumor regions in the breast in DCE-MRI, enabling the generation of the pathophysiological mapping of the tumor habitats and allowing their posterior analysis. In Section 3, we present the results obtained by applying the methodology developed in this work. Section 4 discusses these results regarding the application of the proposed methodology. Finally, Section 5 concludes this article.

2. Materials and methods

In this section, we describe the proposed methodology, which comprises three steps. In the first step, we acquire the images from the database. In the second, we describe the segmentation of the breast in DCE-MRI. Finally, in the third step, we demonstrate how the generation of tumor habitats is performed. Fig. 1 shows the steps of this methodology.

2.1. Database DCE-MRI

The database used in this study was the *Quantitative Imaging Network Collections* (QIN) Breast DCE-MRI [13,14], which is maintained by a US university center, and were acquired using a Siemens 3T TIM Trio. This database aims to evaluate the variations in the evaluation of DCE-MRI of the response of breast cancer to neoadjuvant chemotherapy. The dataset contains DCE-MRI of 10 patients. Each patient has two exams, volumes V1 and V2 with an interval of approximately 30 days, for a total of 20 DCE-MRI exams. Out of these cases, only 3 patients had complete pathological responses (pCRs) and 7 had no response (non-pCRs) [13].

The acquisition parameters of the DCE-MRI include an inclination angle of 10°, 2.9/6.2 ms TE/TR, a parallel imaging acceleration factor of two, 30–34 cm field of view of the object (FOV), 320320 plane matrix and 1.4 mm cut thickness. The acquisition of the exams took 10 min for a set of 32–34 image volumes of 112–120 slices each, with temporal resolution 18–20 s, for a total of 640 exams on average. The Gd (HP-DO3A) [ProHance] CA IV injection (0.1 mmol/kg at 2 mL/s) by a programmable power injector was programmed to begin after the acquisition of two image volumes, followed by a 20 mL jet [13].

In this work, we defined the exam as the procedure performed by the magnetic resonance (MR) equipment to generate the DCE-MRI. The DCE-MRI refers to the image generated by the MR.

2.2. Breast segmentation

In breast segmentation, preprocessing is performed to remove unwanted elements from the DCE-MRI, as described in Section 2.2.1. Subsequently, a binary mask is created in order to extract only the voxels belonging to the breasts. This process is detailed in Section 2.2.2, and Fig. 1 shows the steps performed in breast segmentation.

2.2.1. Preprocessing

Initially, we create a 50% cut in volume (Fig. 1 (cut)), through the Y-axis, so as to eliminate unwanted tissues/organs, such as the heart, arteries, and lungs, among others, that lie below the breasts. These organs may be confused with the injury candidate regions during the CA injection. After the cut is made, we employ rigid registration [15,16], in order to adjust the dimensions, spacing, and other imperfections introduced by the acquisition process. To perform the registration, the first DCE-MRI (pre-contrast) examination was defined as a fixed image to register the remaining images.

To generate image T_2 (post-contrast start), we used the highest intensities of the intermediate images between t_1 and t_n; that is, $T_2 = max(t_2, ..., t_{n-1})$, where $T = [t_1, t_2, t_3, ..., t_n]$ represents the DCE-MRI generated by the exams over time and n is the number of exams performed on the patient. Image T_3 (post-contrast end) is represented by the last DCE-MRI performed in the examination; therefore, $T_3 = t_n$. This process was automated, and is shown in Fig. 1.

2.2.2. Binary mask

The following step was the creation of the binary mask to extract only the breast regions. This process is performed as follows. First, apply Otsu [17] to T_1 (pre-contrast) in order to remove the background (Fig. 2(b)), separating the breast regions and facilitating the generation of the binary mask (Fig. 2(d)). Then, $P_1(x_{P_1}, y_{P_1})$ represents the center point of the volume (Fig. 2(c)), where the coordinates on the X, Y, and Z-axis have the smallest values and the value of the voxel is nonzero. x_{P_1} is the central coordinate of the X-axis and y_{P_1} is the coordinate of the smallest value traversed along the Y-axis in all the slices with nonzero voxel values.

To find $P_{1(x_{P_1}, y_{P_1})}$, the following steps are performed: *i)* find the width of the image on the X-axis; *ii)* bisect the width of the image and find the central position on the X-axis. From this center, traverse the Y-axis, drawing a vertical line (Fig. 2(c) yellow line) until a voxel value other than 0 is found; these values are assigned to the coordinates x_{P_1} and y_{P_1}. This process is repeated in all slices until the smallest values for x_{P_1} and y_{P_1} are found, with the intention of obtaining the lowest position of these coordinates between the slices.

The point $P_{2(x_{P_2}, y_{P_2})}$ represents the lower left point of the breast in the volume, where x_{P_2} is the minimum value of the X-axis coordinate with voxel value other than 0 and y_{P_2} is the maximum value of the Y-axis coordinate with voxel value other than 0. $P_{3(x_{P_3}, y_{P_3})}$ represents the lower point at the right of the breast in the volume, where x_{P_3} is the maximum value of the X-axis and y_{P_3} is the maximum value of the Y-axis, where the value of the last voxel is different from 0. These two

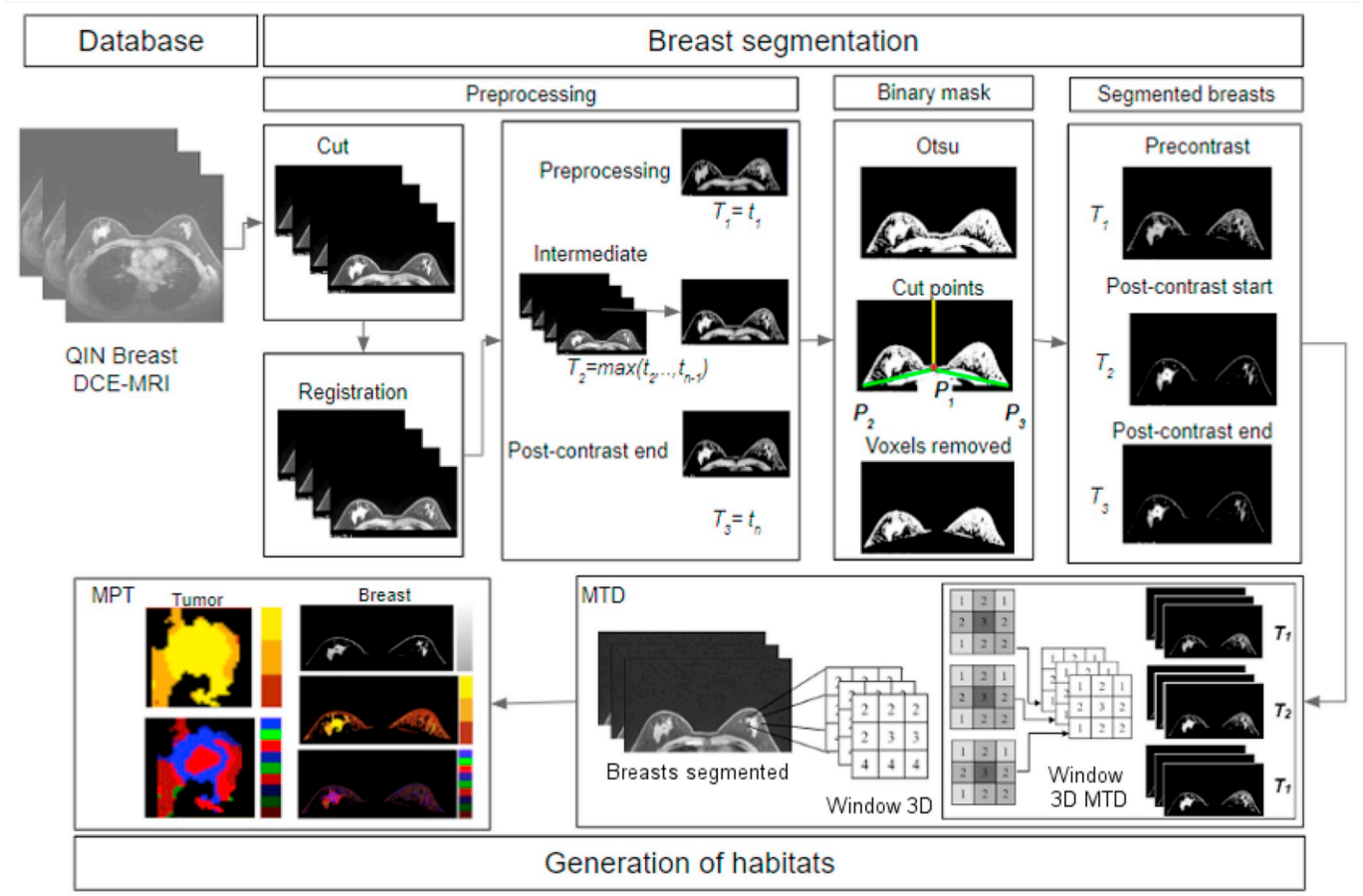

Fig. 1. Methodology steps.

points (P_2 and P_3) are shown in Fig. 2(c).

After identifying the three points P_1, P_2, and P_3, two lines are drawn. The first line is $R_{(P_1,P_2)}$, which links P_1 to P_2, and the second is $R_{(P_1,P_3)}$, which connects P_1 to P_3; both lines are shown in green in Fig. 2(c). Once this is done, all the voxels $V_{(i,j,k)}$ that lie below these two lines, calculated according to Equations (1) and (2), are removed in adherence to

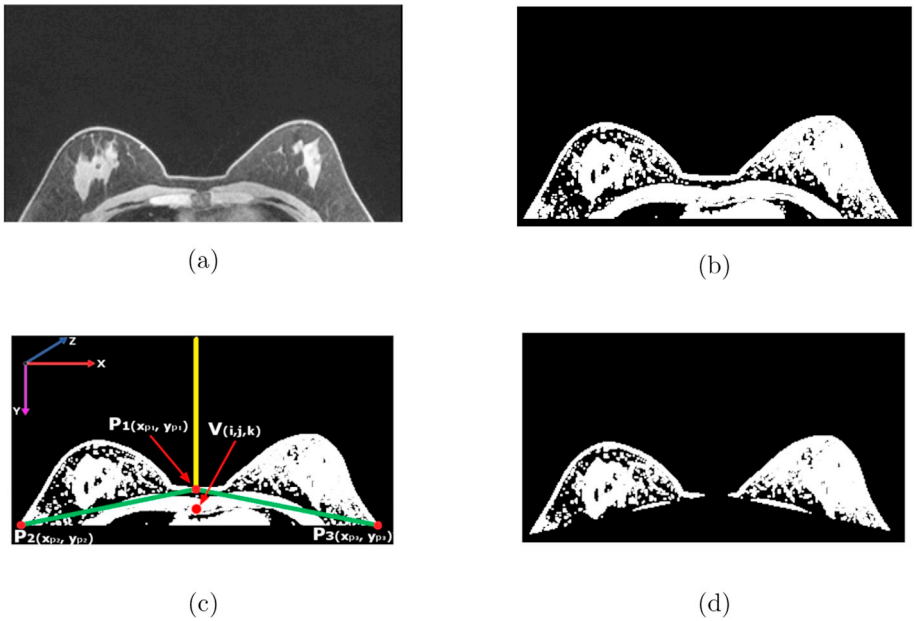

Fig. 2. Illustration of binary mask generation processing: a) Pre-contrast input image; b) result of Otsu applied in (a); c) cut image for voxels removal: X, Y, and Z represent the directions of the volume axes; the points $P_1(x_{P_1}, y_{P_1})$, $P_2(x_{P_2}, y_{P_2})$ and $P_3(x_{P_3}, y_{P_3})$ indicate the cutoff points of the volume; the yellow line shows how P_1 was found; the green lines indicate the area of the voxels to be removed and the connection of (P_1, P_2) and (P_1, P_3); $V_{(i,j,k)}$ represents a voxel below the two green lines, which will be removed; d) image of the binary mask resulting from the removal of voxels in (c).

the constraints of Equations (3) and (4).

$$R_{(P_1,P_2)} = V_j\left(y_{P_1} - y_{P_2}\right) + V_i\left(x_{P_2} - x_{P_1}\right) + \left(x_{P_1}y_{P_2}\right) - \left(y_{P_1}x_{P_2}\right) \quad (1)$$

$$R_{(P_1,P_3)} = V_j\left(y_{P_1} - y_{P_3}\right) + V_i\left(x_{P_3} - x_{P_1}\right) + \left(x_{P_1}y_{P_3}\right) - \left(y_{P_1}x_{P_3}\right) \quad (2)$$

$$R_{(P_1,P_2)} < 0 \quad (3)$$

$$R_{(P_1,P_3)} > 0 \quad (4)$$

where V_i and V_j are the positions of the row and column of the current voxel whose removal is under consideration. x_{P_1} and y_{P_1} are the coordinates of the central point P_1. x_{P_2} and y_{P_2} represent the coordinates of the lower left-hand point of the breast P_2, and x_{P_3} and y_{P_3} are the coordinates of the lower right-hand point of the breast P_3.

Fig. 2 shows the results of this process, which yields the image masks T_1, T_2 and T_3 with the segmented breasts. These will serve as input to the MTD detailed in Section 2.3.1.

2.3. Generation of habitats

In this section, the generation of tumor habitats is described, and to this end, two techniques are applied: MTD and MPT. The first performs an improvement in the breast images, enhancing the regions of the CA and generating a new representation of the image. The second uses this new representation generated by MTD and generates the habitats of the tumor.

2.3.1. Molecular texture descriptor (MTD)

MTD is a novel volume representation based on texture. MTD is based on the elements of organic chemistry, as if they were the molecules of a tissue. By making an analogy, we can say that a voxel represents the chemical elements and a group of voxels represents the cell. Table 1 presents this relationship.

Given a segmented breast image (Fig. 3(A)), a 3D window/cell (Fig. 3(B)) is extracted from this image and applied to Equations 5 and 7, according to (Fig. 3(c)), which yields the average molecular mass M_m of all the chemical elements E_i of that region.The result is then inserted in the center of the window. After the process is performed on all the voxels of the window, a new representation of the image is generated, as shown in Fig. 3(D).

By the end of this step, a new representation of the image is generated. With this new image, we can generate two values of texture characteristics: the average molecular mass and the molecular mass, given by Equations (5) and (6), respectively.

$$M_m = \frac{1}{n}\sum_{i=1}^{n} MM_{E_i} \quad (5)$$

$$M = \sum_{i=1}^{n} MM_{E_i} \quad (6)$$

$$MM_{E_i} = N_{E_i}\, m_{E_i} \quad (7)$$

where, MM_{E_i} represents the molecular mass of the element in the window/3D cell in question, i.e., the molecular mass of the voxel, given by the product of the number of voxels and their value. N_{Ei} corresponds to the number of voxels of the same density, and m_{Ei} is the atomic mass of the chemical element, which represents the density value of voxel. This process is used in the application of MTD.

By applying MTD, it is possible to improve the pixels of the image according to their vicinity, giving emphasis to the texture of the breast tissue. This descriptor allows us to highlight the structures of the CA and simultaneously remove unwanted noises, depending on their neighborhood. Fig. 3 shows the results of applying MTD.

MTD is applied to images T_1, T_2 and T_3, providing the input to the pathophysiological mapping of texture, as described in Section 2.3.2.

2.3.2. Pathophysiological mapping of texture in DCE-MRI (MPT)

This section describes the application of the pathophysiological mapping of texture in DCE-MRI, which consists of the study of the physiological mechanism of cellular, organic, and systemic diseases and pathologies, considering the alterations that arise in the normal functioning of such tissues [6,11,18]. In this work, we used this study to analyze the pathophysiological behavior of the CA in the breast, in order to identify the regions that suffered the most changes with CA action.

The use of MPT proposed in this work is intended to automatically find the tumor-suspect regions, analyzing the behavior of the CA action in the images T_1, T_2 and T_3, namely, the precontrast, postcontrast, and final postcontrast, respectively. These images are generated during the MTD process described in Section 2.3.1.

By definition, we assume that $T(t) = \{T(1), T(2), T(3)\}$, which represents the images in the time interval t, where $t = \{1,2,3\}$. To find the tumor-candidate regions, the intensities of each voxel are considered.

The initial pre-contrast (IE) represents the fill signal of the CA [11]. This value describes the initial CA action during T_1 and T_2, after injection. Depending on the IE value calculated in Equation (8), the CA can be slow, medium, or fast [11].

The initial post-contrast (PIE) represents the initial signal of the CA action, soon after injection [11]. This value describes the behavior of the CA during the post-contrast and is calculated according to Equation (9).

The final post-contrast (SER) indicates the final signal of the CA action [11,18,19], describing its behavior until the last instant after injection. The SER is calculated by Equation (10).

$$pre - contrast\,(IE) = \frac{T(2) - T(1)}{T(1)} \quad (8)$$

$$initial - post - contrast\,(PIE) = \frac{T(3) - T(2)}{T(2)} \quad (9)$$

$$final - post - contrast\,(SER) = \frac{T(2) - T(1)}{T(3) - T(1)} \quad (10)$$

Applying Equations (8)–(10) to $T(1)$, $T(2)$ and $T(3)$, we have assembled the 3 TP curves [11,20], as shown in Fig. 4. This is a method of analysis to determine the filling and emptying of the CA over time, where t_1, t_2, and t_3 represent the images in time. Fast, normal, and slow,

Table 1
Analogy of MTD representation nomenclature.

Equations	Chemical	MTD
$E_i = f_i(x, y, z)$	Chemical element	Voxel
$C = [P_i, ..., P_n]$	Cell	Group of voxels
M_m	Average molecular mass	Sum of voxels multiplied by their quantity of the same density, divided by the total number of voxels
M	Molecular mass	Sum of voxels multiplied by their quantity of the same density
MM_{E_i}	Molecular mass of element	Product of the number of voxels and their value
N_{E_i}	Number of elements	Number of voxels of the same species
m_{E_i}	Atomic mass of the chemical element	Voxel density value
n	Number of cell elements	Number of voxels of the same density of the region

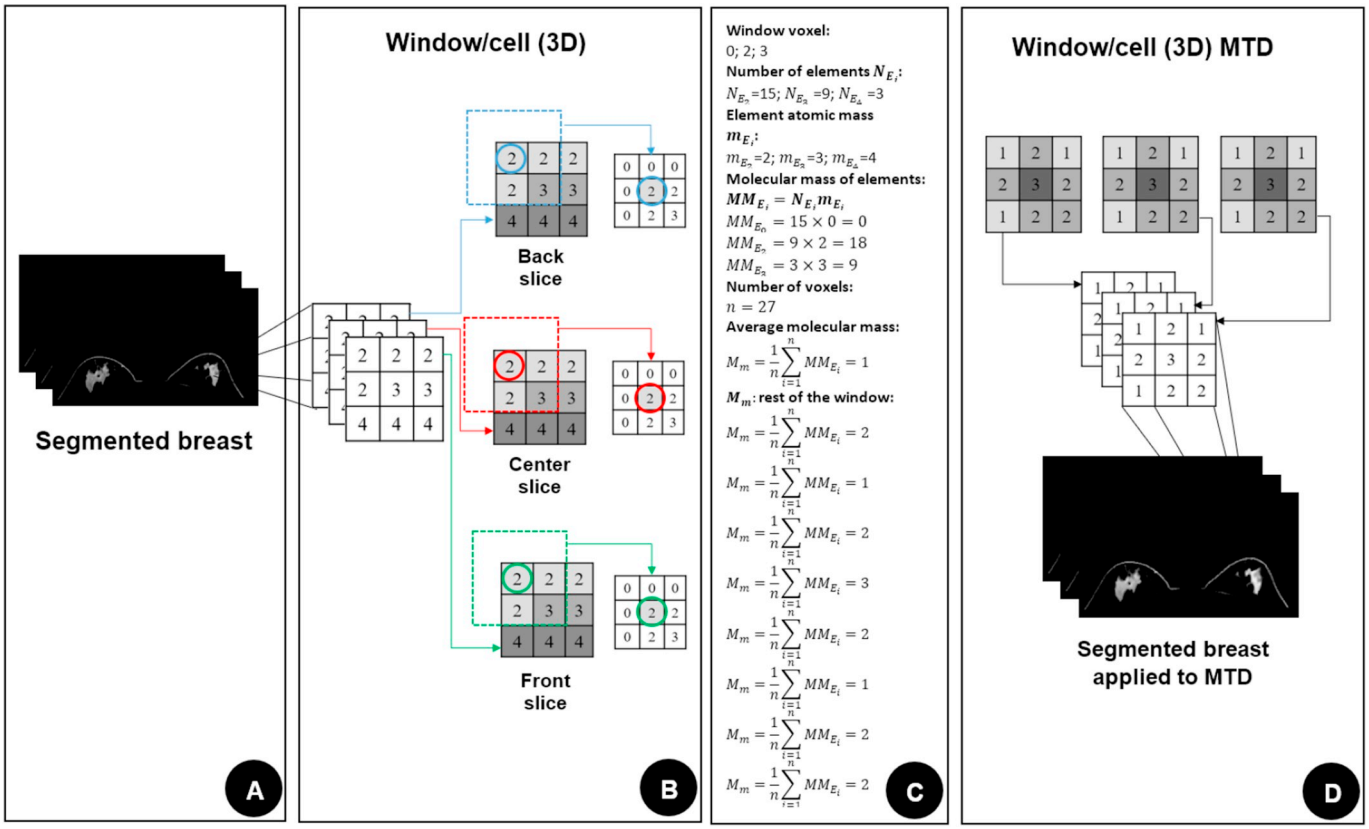

Fig. 3. MTD application procedure: A) Segmented breast entry image; B) window/3D cell extracted from (A) and its back, center, and front slices, with their respective voxels and indicated in blue, red, and green is a specific region with its neighborhood; C) calculation of the MTD in the window/3D cell, presented in (B) with the values of voxels 0, 2, and 3; D) result of the window/3D cell after application of MTD, which highlights the contrast agent in the segmented breasts.

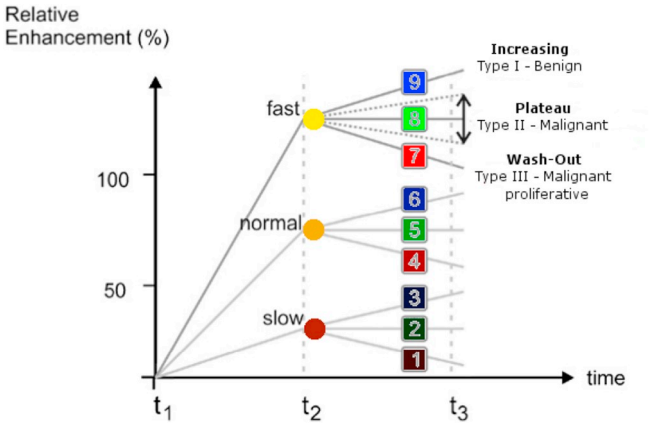

Fig. 4. 3 TP curve method: t_1, t_2 and t_3 represent the images in time. The three classes slow, normal, and fast identify the filling of the CA; The nine color-hue combinations (1 the 9) determine the subclasses of the CA emptying that can be Increased, Plateau, and Wash-Out, which are classified as type I - benign, type II - malignant, and type III - malignant proliferative.
Source: Adapted from Preim et al. [20].

mean the three classes of CA behavior during filling, between t_1 and t_2. The result of this process is shown in Fig. 5(d).

The 9 color/hue combinations (1–9) in Fig. 4 represent the behavior of the CA during the emptying between t_2 and t_3 for each of the 3 classes (fast, normal, and slow), with each class able to assume type I - benign, type II - malignant, and type III - malignant proliferative, which are increasing, plateau, and washout, respectively. These 9 types represent the subclasses of the habitats found in the tumor, as shown in Fig. 5(e).

This curve allows us to illustrate the behavior of the CA action within the regions of the breast. However, *PIE* defines the output value of the CA for the 3 TP curve plot (Fig. 4) and *SER* defines the coding to color the regions of the tumor, generating their habitats. In this work, we used IE to initially define how the CA filling was performed in certain regions, which can be slow, medium, or fast, and the *SER* value is used to define the emptying (increasing, plateau, or washout) of the CA in tumor regions. The result of this process can be visualized in Fig. 5.

To find the candidate tumor regions in a DCE-MRI of the breast, those with the largest IE fill value are chosen as *IE*. In Fig. 5(b), the IE result can be visualized in the regions where the CA action can be slow, normal, and fast indicated by brown, orange, and yellow, respectively. These regions represent where the CA was more active in the breast, and the yellow regions are those that are most likely to be malignant, because they represent regions where the CA showed rapid filling. Therefore, they are considered suspect. These yellow regions are then extracted, giving rise to tumor candidates, and the MPT is performed again, only on those candidate regions to be analyzed individually. Fig. 5(d) shows the *IE* representing the filling of the CA, and *PIE* and *SER* represent emptying, as shown in Fig. 5(e).

Based on the literature, we can say that values of SER less than 1 represent persistent (increasing), while those greater than 1 indicate washout curves [18]. However, the following criteria were used to define the behavior of the CA during emptying (increasing, plateau, or washout): *i*) $SER \geq 1.2$ indicates washout (red hue), representing type III - malignancy; *ii*) $(0.9 \leq SER < 1.2)$ indicates plateau (green hue), represents persistence of type II - malignancy; *iii*) $SER < 0.9$ indicates increasing (shades of blue), defining type I - benignity [11,19,20].

Our methodology classifies tumors based on the 3 TP curve method [11,18,20]. This method analyzes the behavior of the CA during its filling and emptying as soon as it is injected into the bloodstream. It is

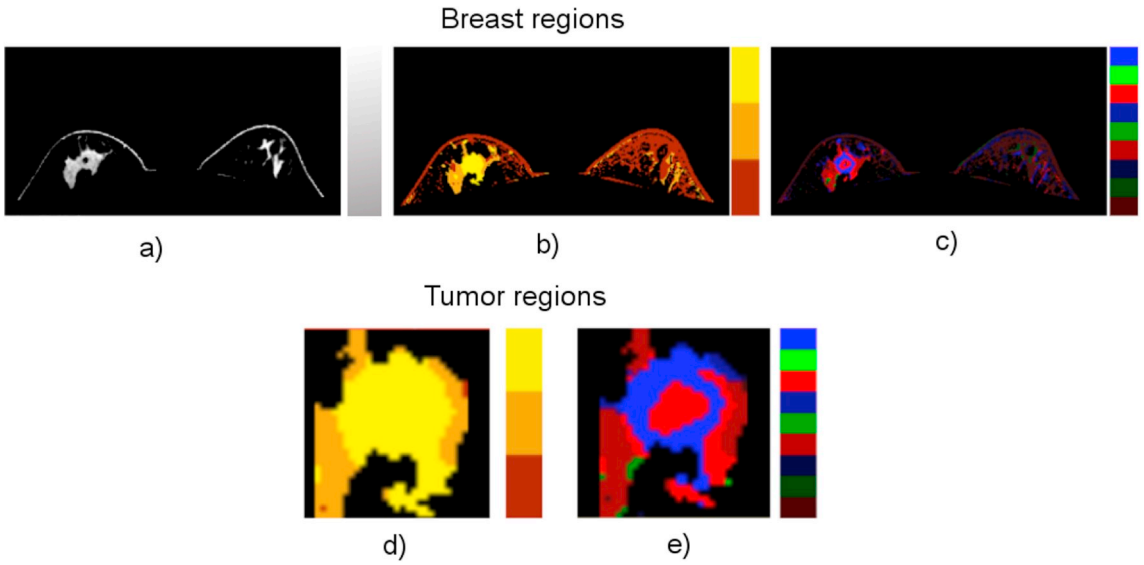

Fig. 5. Result of MPT processing: a) Image of the entry breast; b) exit breast image with three color regions of the CA filling (brown = slow, orange = normal, and yellow = fast); c) image of the output breast with the nine color hue (blue, green, and red), representing the subclass of the CA emptying; d) image of the tumor with the three color classes (brown, orange, and yellow) representing the CA filling; e) image of the tumor with the nine subclasses with color hue (blue, green, and red), in different intensities, representing the emptying of the CA.

known from the literature that in benign tumors, CA can present fast, normal, or slow behavior during its filling. However, its emptying can only be increasing (type I benign), because benign tumors have the characteristic of continuing to increase the voxel density upon the exit of the CA. In Fig. 4, numbers 3, 6 and 9 with blue hues indicate the 3 TP curves of benign tumors.

The filling behavior of CA in malignant tumors can also be fast, normal, or slow. However, its emptying can be defined in two ways. The first is characterized as plateau (type II - malignant), which is when the CA empties in a non-abrupt manner; that is, when the voxel density does not show significant variation. This result is shown in Fig. 4 by numbers 2, 5, and 8, with green hues, exemplifying 3 TP curves of malignant tumors. The second is defined as washout (type III malignant proliferative), which is characterized by the CA leaving quickly during its emptying [11,19,20]. In this case, the exit of the CA brings about a sudden change in the voxel density value, as shown in Fig. 4 by numbers 1, 4 and 7 with red hues.

In Fig. 5, we can visualize the result of this process, together with all the habitats generated through the application of MTD and MPT.

2.4. Segmentation validation metric

To evaluate the segmentation of the methodology, we use the accuracy, sensitivity, and specificity as metrics. Another metric used to evaluate our method was the volumetric similarity (VS). This metric is calculated in Equation (11) and measures the absolute volume of a segmented region compared to another segmentation [21].

$$VS = 1 - \frac{|FN - FP|}{2TP + FP + FN} \tag{11}$$

where *FN* FN is the false negative rate, *FP* is the false positive rate, and *TP* is the true positive rate. In our work, we used VS to evaluate the region segmented by the proposed method with base marking.

3. Results

The tumors analyzed in this study are all malignant and are undergoing chemotherapy. The results presented do not consider the temporal analysis of the exams; that is, all the cases are analyzed individually. The database is composed of 10 patients, and there are two exams (V1 and V2) for each patient, for a total of 20 tumors. The results of this study were very promising, with 100% of the cases of tumors in the breast identified. The results of the segmentation evaluation metrics were 99.95%accuracy, 71.07% sensitivity, 99.98% specificity, and 77.75% VS. In addition, it was possible to classify the tumor malignancies, with 6 malignant type III (washout) and 14 malignant type II (plateau), for a total of 20 cases (all malignant). Here, we provide details of how these results were obtained.

In Fig. 6(a), we can see the result of the 3 TP curves of all the cases under study. Analyzing the graph, we highlight curve 18, which refers to case BC15-V2, because it was the only one with the CA slow fill. Analyzing the graph of Fig. 6(b), and with reference to the result of the specific case BC01-V2, we highlight curve 7, because it was the only one that had increasing emptying, that is, represented a benign habitat.

Initially, the regions generated by MPT were analyzed. These regions present the possible tumors in the breast and were acquired based on MTD (Section 2.3.1) and on the 3 TP curve (Fig. 4), using only the *IE* filling as a parameter of inclusion of those regions of the breast. Then, all regions in which the *IE* value (Fig. 7 (b), Fig. 7) was fast (yellow) were considered as possible breast tumors.

Analyzing the results of the MPT application to the suspect region, we can verify that these regions stand out, considering the specialist's marking (Fig. 7(a)), demonstrating the CA's behavior when penetrating the breast (Fig. 7(b)). The IE can be slow, medium, and fast, corresponding to the colors brown, orange, and yellow respectively. This was only possible owing to the MTD, which was able to enhance the regions of the tumor, thereby lending more prominence to the CA within the breast.

In Fig. 7(c), we can see the results of the CA behavior within the tumor during the filling process, as calculated by *IE*, where the colors brown, orange, and yellow correspond to slow, medium, and fast, respectively. Fig. 7(d) shows the result of the behavior of the CA within the tumor during the emptying process as calculated by *SER*, and predicts its behavior, which can be classed as increasing, plateau, or washout, as represented by the 9 hues of blue, green, and red.

Fig. 8(a) shows a boxplot of the CA behavior during filling. By analyzing the graph, we notice that the largest volume corresponds to 39.403% of the tumor, and thus we can infer that most of the tumor was filled with CA media. Fig. 8(b) shows a boxplot regarding the CA behavior during emptying and, in this graph, it was inferred that the

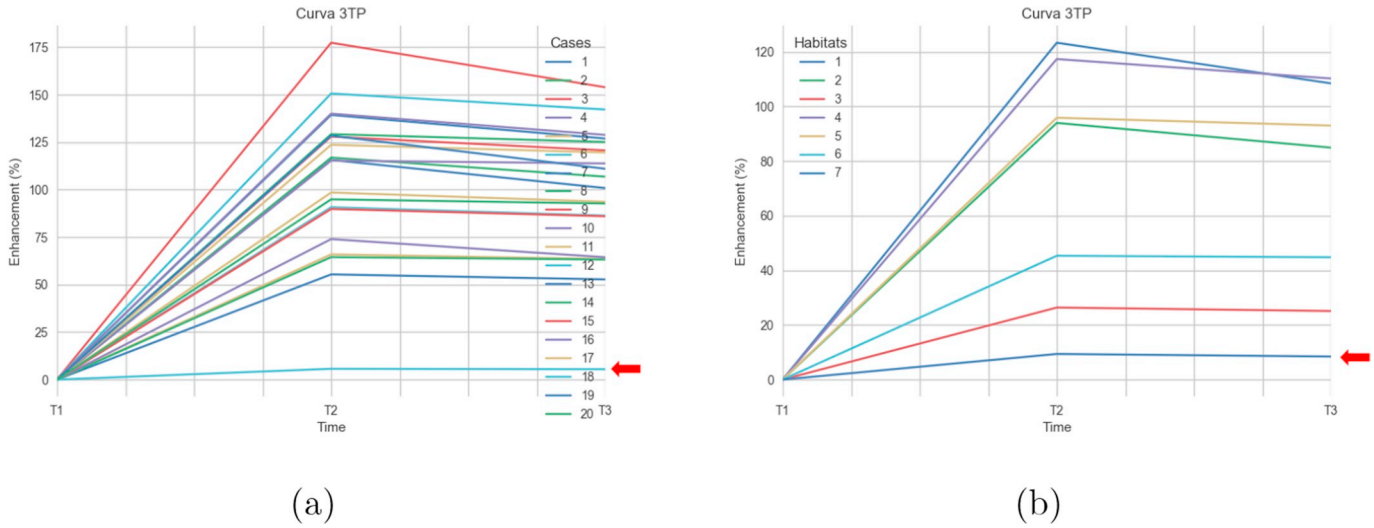

Fig. 6. Result of 3 TP Curves: a) All cases; b) case BC01-V2.

largest volume corresponds to 68.11% of the tumor, characterized as malignancy type II (plateau).

One may notice that MTD was able to enhance the regions of the tumor where the CA was more active (Fig. 9(a)), which allowed MPT to separate all regions of the breast, and thus highlight possible tumor regions (Fig. 9(b)). However, these same regions were again subjected to the MPT to analyze their internal regions, except that this time all the calculations were performed using Equations (8)–(10), with *IE* for the filling and *SER* for the emptying of the CA. Fig. 9 (from c to i) show the results of all the habitats generated by the MPT.

According to Table 2, we can verify that during the CA entering, 1 slow, 9 medium, and 10 fast cases were found, adding up 20 cases. Therefore, we can conclude that most of the cases studied exhibited fast filling behavior. Analyzing the CA exiting, 6 washout, 14 plateau, and no increasing cases were detected. By combining these two results, 3 cases (1, 3, and 19) had fast filling and washout emptying, and it can be inferred that all these cases are type III malignant, because tumors that have fast input and output are suggestive of proliferative or aggressive malignancy.

Another analysis that can be performed with respect to Table 2 relies on the absence of cases suggestive of benignity (increasing - type I), culminating in what was said previously, that the database only has malignant tumors under treatment. Therefore, the MPT was able to automatically detect all tumors and reached its goal of performing the pathophysiological mapping of tumor habitats.

In Table 3, we present the results of the MPT application for the case BC01-V2, because it presented the various types of filling and emptying of the CA inside the tumor. Analyzing these data, it can be stated that seven habitats (Fig. 9) were found, which were mapped with 2 fast, 2 medium, and 3 slow cases during the filling, and 3 washout, 3 plateau, and 1 increasing cases during the emptying. Therefore, analyzing the CA emptying behavior in the largest tumor habitats, we can state that 31.76% were washout, 68.11% were plateau, and 0.12% were increasing. Summarizing these percentages, we conclude that most of the tumor consists of washout and plateau habitats. Therefore, we can characterize this tumor as suggestive of type II - malignancy. The results of this case (BC01-V2) are shown in Figs. 7 and 9.

Considering the results of this work, we can state that the methodology represents an aid to the treatment of patients suffering from breast cancer, based on DCE-MRI exams.

4. Discussion

In recent years, several studies have shown that the analysis of tumor behavior in DCE-MRI has aided in the search for better strategies in the treatment of cancer. The application of pathophysiological mapping techniques appears to be an efficient and effective solution to find new strategies in the treatment of cancer patients, allowing specialists to more safely make changes during treatment.

In this work, we presented a novel approach to the pathophysiological mapping of breast tumors in DCE-MRI, using the MTD and MPT. The former is used as an image texture descriptor capable of highlighting the CA regions, generating a new representation and extracting features. The latter, used to generate the pathophysiological mapping

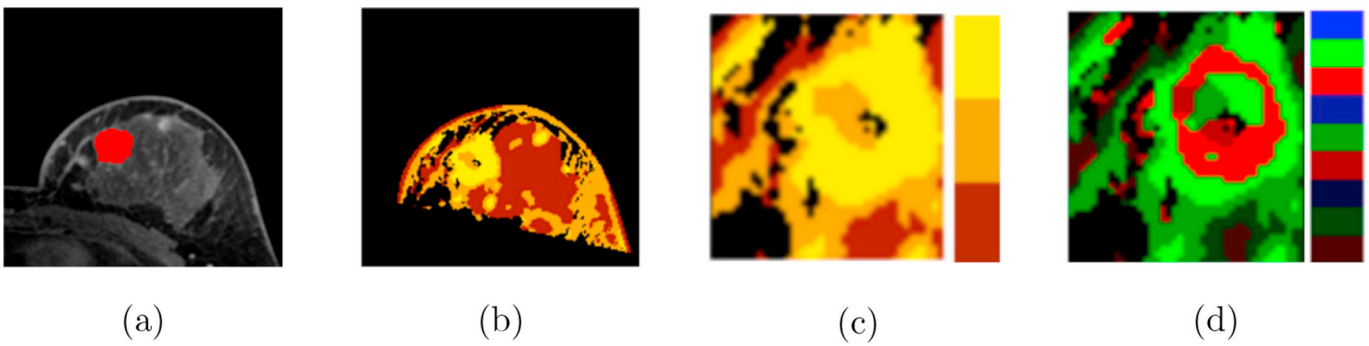

Fig. 7. Result of MPT in case BC01-V2: a) Image T_2 of the breast with the tumor marked in red by the specialist; b) output image of the breast with the three color regions of the CA filling (brown = slow, orange = normal, and yellow = fast); c) image of the tumor extracted from the breast with the three regions (slow, normal, and fast) referring to the CA filling; d) image resulting from the tumor with the nine color hues (blue, green, and red), representing the subclass of the CA emptying.

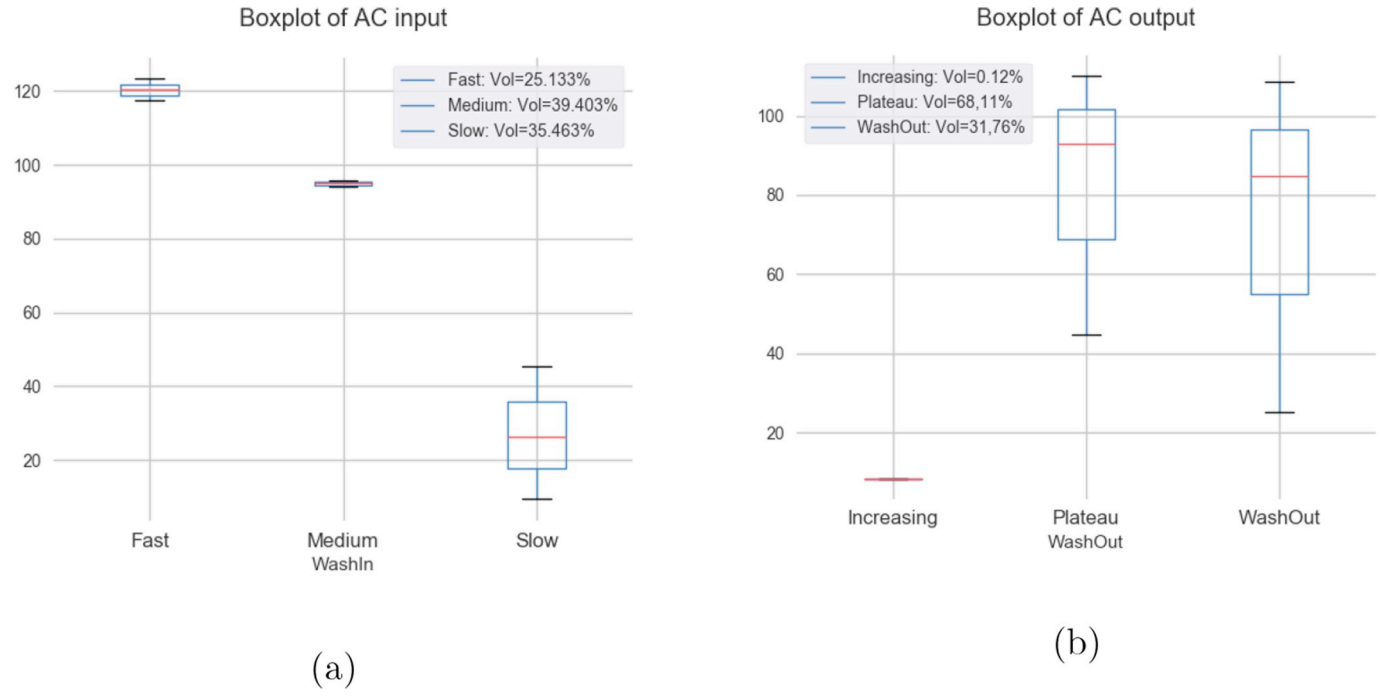

Fig. 8. Result of boxplot applied to case BC01-V2: a) boxplot of the CA filling; b) boxplot of the CA emptying.

based on the behavior of the CA, allows the automatic discovery of tumor habitats in the breast.

Among the results found, we highlight case BC01-V2, in which, as seen in Fig. 7(b), the method was able to segment the tumor automatically according to the specialist's marking. Furthermore, it could analyze the tumor habitats, allowing the identification the type of behavior performed by the CA. This shows that the method is efficient at finding breast tumor habitats in DCE-MRI, suggesting new follow-up strategies during the treatment of cancer.

A negative analysis of the methodology was the case BC15-V2, because the region found during tumor detection was larger than expected, considering the specialist's label. This occurred due to two possible factors:

i) During the process of finding the tumor candidate regions, we noticed that the CA had dispersed in almost the whole breast, as shown in Fig. 10(a). This dispersion caused the CA to fragment into several regions of different slices, apparently separate. However, all the slices of the possible tumor regions are connected to each other, as their volume in Fig. 10(e) shows. Therefore, when the tumor candidate region is extracted, its volume is larger than that indicated by the specialist (Fig. 10(c)).
ii) As the candidate region has a large volume, involving almost the whole breast, when the MPT generates the habitat mapping, it is

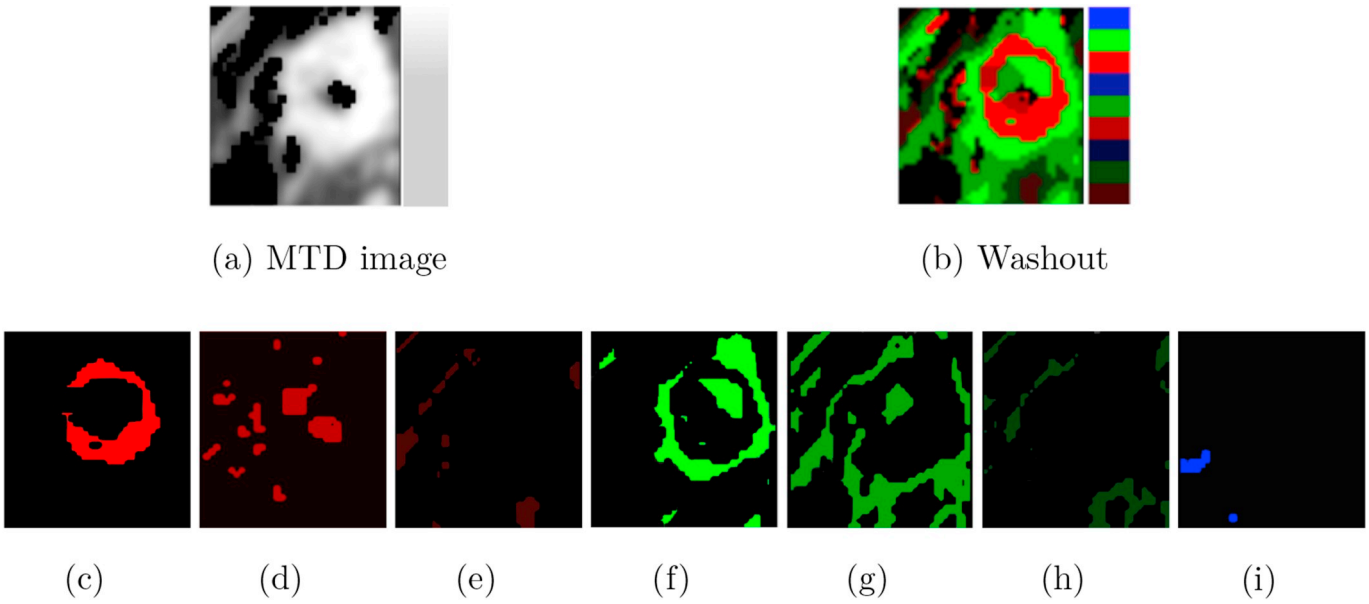

Fig. 9. Result of the habitats generated by the MPT of case BC01-V2: a) original tumor image (T_2) with MTD; b) colorful tumor habitats generated by MPT, representing the behavior of the CA during emptying; c) habitat fast and washout; d) habitat medium and washout; e) slow habitat and washout; (f) habitat fast and plateau; g) habitat medium and plateau; h) habitat slow and plateau; i) habitat slow and increasing.

Table 2
Result of the application of MTD and MPT to all cases of the dataset.

Cases	IE	PIE	SER	Input CA	Output CA	Malignancy (Type)
BC01-V1	**1.15625**	**−0.128019**	**1.31361**	**Fast**	**WashOut**	**III**[a]
BC01-V2	1.1686	−0.0857909	1.18935	Fast	Plateau	II
BC05-V1	**1.77333**	**−0.132212**	**1.26066**	**Fast**	**WashOut**	**III**[a]
BC05-V2	1.15278	−0.0129032	1.02469	Fast	Plateau	II
BC06-V1	0.659218	−0.037037	1.1028	Medium	Plateau	II
BC06-V2	0.640719	−0.167883	1.7541	Medium	WashOut	III
BC08-V1	0.553691	−0.0475162	1.15385	Medium	Plateau	II
BC08-V2	0.64486	−0.0198864	1.05344	Medium	Plateau	II
BC10-V1	1.27891	−0.0567164	1.11243	Fast	Plateau	II
BC10-V2	0.739645	−0.129252	1.43678	Medium	WashOut	III
BC12-V1	1.23595	−0.0326633	1.0628	Fast	Plateau	II
BC12-V2	1.5061	−0.0559611	1.10268	Fast	Plateau	II
BC13-V1	0.771277	0.00600601	0.986395	Medium	Plateau	II
BC13-V2	1.29197	−0.0318471	1.05988	Fast	Plateau	II
BC14-V1	0.897849	−0.0424929	1.09868	Medium	Plateau	II
BC14-V2	1.4	−0.0801282	1.15924	Fast	Plateau	II
BC15-V1	0.984848	−0.0496183	1.11111	Medium	Plateau	II
BC15-V2	0.0566038	−0.0392857	3.75	Slow	WashOut	III
BC16-V1	**1.28387**	**−0.135593**	**1.31788**	**Fast**	**WashOut**	**III**[a]
BC16-V2	0.948718	−0.0230263	1.04965	Medium	Plateau	II

[a] Proliferative or aggressive malignant.

Table 3
Result of habitats generated by the application of MTD and MPT, considering case BC01-V2.

Habitats	IE	PIE	SER	Input	Output	Vol	% Vol
Fig. 9(c)	1.23353	−0.120643	1.2795	Fast	WashOut	4197.72	9.319
Fig. 9(d)	0.939759	−0.096273	1.248	Medium	WashOut	2803.75	6.225
Fig. 9(e)	0.263804	−0.048543	1.30303	Slow	WashOut	7306.51	16.221
Fig. 9(f)	1.17365	−0.060606	1.12644	Fast	Plateau	7123.17	15.814
Fig. 9(g)	0.958823	−0.03003	1.06536	Medium	Plateau	14944.9	33.179
Fig. 9(h)	0.453488	−0.012	1.04	Slow	Plateau	8611.97	19.119
Fig. 9(i)	0.09375	−0.10	−6	Slow	Increasing	55.3164	0.123

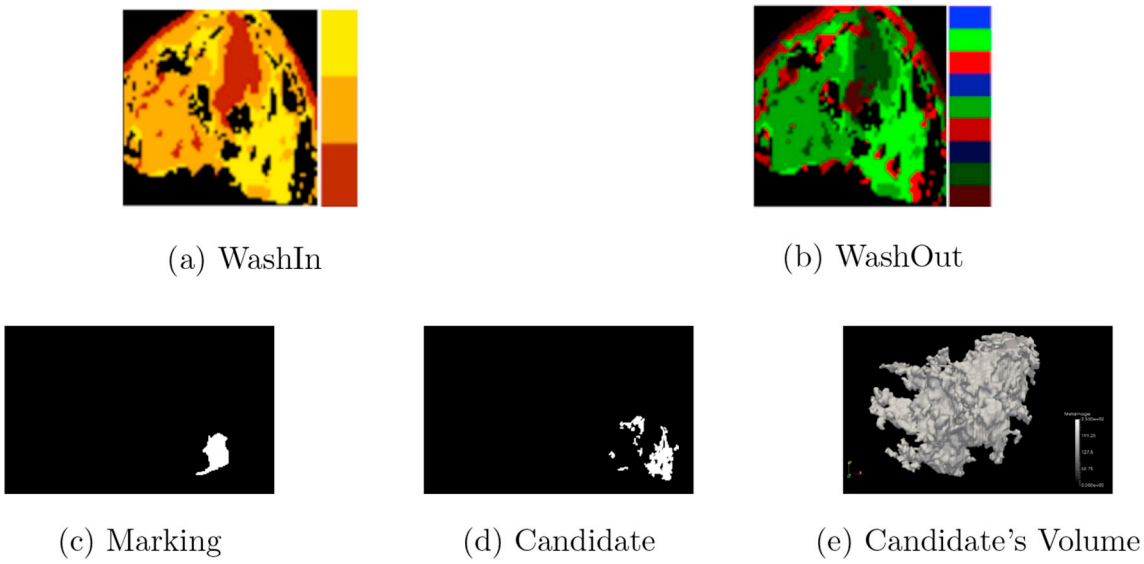

Fig. 10. Result of MTD and MPT-DCE-MRI in case P15-1: a) breast washin image; b) washout result in the tumor; c) marking of the tumor performed by the specialist; d) tumor candidate region detected by the methodology; e) volume of the candidate region, demonstrating that the slices are connected.

applied to the almost the whole breast, resulting in a larger region than that marked by the specialist, Fig. 10(c). However, if we disregard the marking, we will see that the methodology can find the tumor, but in a larger proportion than the one marked, Fig. 10(d).

Analyzing the result of the proposed segmentation, we highlight that the metrics of sensitivity and VS show the percentages of 71.07% and 77.75%, respectively. One could imagine that the values are low, but these values are justified by the fact that our methodology is based on the behavior of the CA to segment the lesions, and in some cases, these lesions present a low CA action on the tissue. This means that the tissue region has little vascularity. Moreover, the specialist marked the lesions only with a circle involving the entire lesion, not considering the CA action, as shown in Fig. 11(b). However, our method seeks to detect

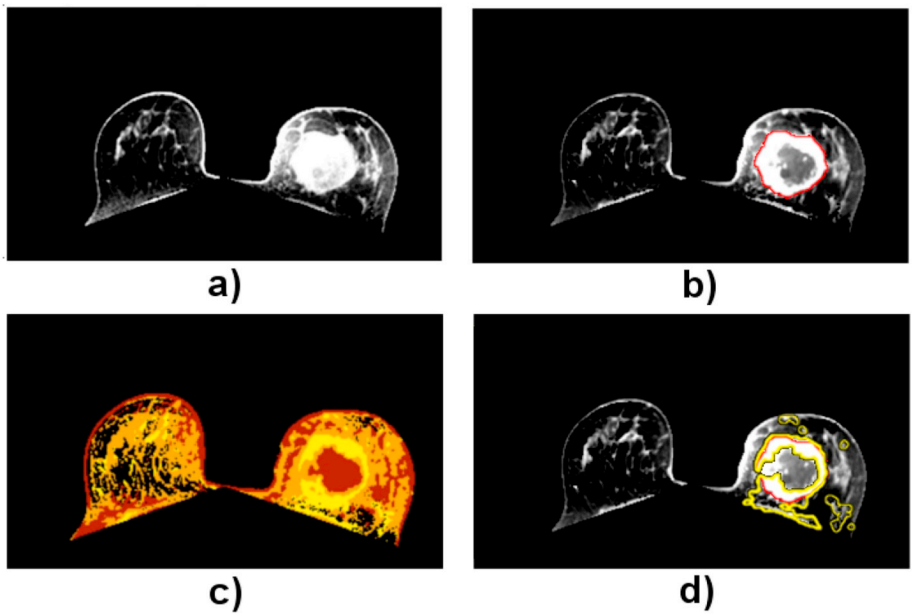

Fig. 11. Illustration of the analysis of the proposed segmentation: a) pre-contrast of the breast; b) post-contrast of the breast with the regions highlighted by CA and marking of the tumor performed by the specialist in red; c) tumor candidate region in yellow detected by the methodology; d) result of the proposed segmentation in yellow, overlap on the marking of the base in red.

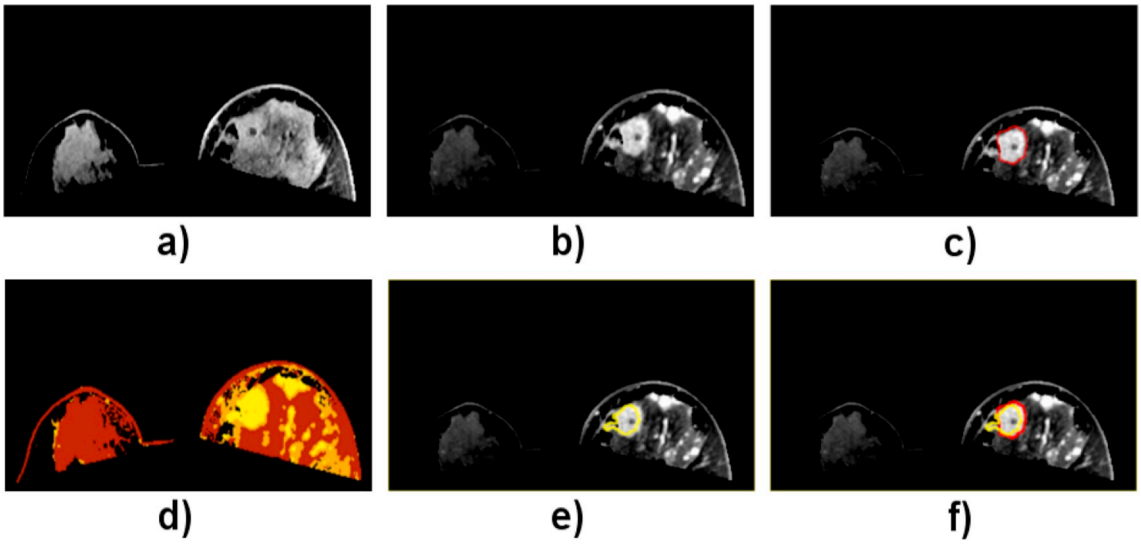

Fig. 12. Analysis of tumor candidates: a) pre-contrast of the breast; b) post-contrast of the breast with the regions highlighted by CA; c) marking of the tumor performed by the specialist in red; d) tumor candidate region in yellow detected by the methodology; e) result of the proposed segmentation in yellow; f) overlap of the proposed segmentation in the dataset marking.

Table 4
Comparison of the techniques used in the proposed methodology compared to other works.

Work	Automatic segmentation		Texture Analysis	Pathophysiological Mapping
	Breast	Tumor		
Hauth et al. [7]				X
Vassiou et al. [6]				X
Karahaliou et al. [11]			X	X
Huang et al. [1]				X
Kim et al. [10]				X
Braman et al. [12]			X	
Banaie et al. [5]			X	
Proposed method	**X**	**X**	**X**	**X**

the habitats of the tumor regions according to the behavior of the CA within the vascularization of the tissues, showing where it had CA action. Fig. 11(d) shows the proposed targeting result in yellow, superimposed on the red base marking. We can see in Fig. 11(b) that the internal region marked by the specialist disregards the CA action.

Our method found other structures in the breast beyond the lesions marked by the base specialist, as shown by the yellow regions in Fig. 12(d). We can consider these findings as false positives. However, these structures considered as false positives have hemodynamic characteristics similar to the marked lesions, as shown in Fig. 12(b), after CA injection.

By consulting a specialist from our research group, we noticed that these structures are also lesions with less visibility and impact than the lesions marked at the base. We believe that the dataset markers are only in primary lesions. We cannot be sure, as there is no information on this fact in the dataset. Fig. 12(c) shows the marking by the specialist in the dataset in red. Fig. 12(e) shows the result of the segmentation in yellow after the elimination of the false positives and Fig. 12(f) shows the

overlap of the proposed segmentation with the base marking, which shows just how similar they are. It is important to note that the dataset includes only malignant tumors.

Because this work analyzes each tumor individually, disregarding the comparison of the two examinations over time (V1 and V2), and considering only the techniques used in the solution of the proposed problem, Table 4 presents a comparison with other related works. As we can see in Table 4, the proposed methodology is the only one that has the automatic segmentation of the breasts. Another difference is the automatic segmentation of the tumor performed in this work, which does not occur in others.

Another advantage presented in this work is the fact that the analysis of the tumor is performed locally based on the action of the CA, allowing us to analyze the different regions of the tumor and classify them individually. However, the other works define the tumor as a single class, disregarding its internal regions. In addition, our work still manages to define, as a percentage, how much volume each class occupies.

There are other studies that use clustering algorithms to try to map tumor habitats. The most common is k-means [22,23], which is based on generating groups through centroids. In contrast, it must be informed of the fixed number of groups, limiting the power of automatic discovery of tumor habitats. In addition, k-means would generate distinct regions for each time period (T_1, T_2 and T_3), as it would not consider the behavior of the CA, making it difficult to analyze the tumor. Therefore, owing to these limitations, it is not possible to compare the proposed methodology with these approaches, because they are totally different.

In summary, by combining MTD with MPT, it was possible to perform the pathophysiological mapping of tumor habitats in the breast in DCE-MRI in a safe and efficient way to determine the behavior of the CA. Consequently, it was possible to characterize the type of malignancy of the tumor during the follow-up of the treatment of cancer patients.

5. Conclusion

In conclusion, in this work, we proposed the automatic detection of tumors in the breast in DCE-MRI and performed the pathophysiological mapping of tumor habitats through the behavior analysis of the CA. This was only possible owing to a combination of two techniques, MTD and MPT, which allowed the mapping of the internal habitats of the tumor. Both of these succeeded in achieving the goal of automatically generating and analyzing the pathophysiological mapping of breast tumor habitats, based on the behavior of the CA, which has aided in the search for new strategies in the treatment of cancer. In a future study, we intend to extend the methodology to perform temporal analysis of tumors, allowing us to determine their behavior (progression, regression, or stabilization) during the treatment.

Acknowledgements

The authors acknowledge financial support from the Federal Institute of Piauí (IFPI), Coordination for the Improvement of Higher Education Personnel (CAPES), and National Council for Scientific and Technological Development (CNPq).

References

[1] W. Huang, X. Li, Y. Chen, X. Li, M.C. Chang, M.J. Oborski, et al., Variations of dynamic contrast-enhanced magnetic resonance imaging in evaluation of breast cancer therapy response: a multicenter data analysis challenge, Transl Oncol 7 (1) (2014) 153–166.

[2] J.P. O'connor, A. Jackson, G.J. Parker, C. Roberts, G.C. Jayson, Dynamic contrast-enhanced mri in clinical trials of antivascular therapies, Nat. Rev. Clin. Oncol. 9 (3) (2012) 167.

[3] A.R. Padhani, K.A. Miles, Multiparametric imaging of tumor response to therapy, Radiology 256 (2) (2010) 348–364.

[4] V.N. Harry, S.I. Semple, D.E. Parkin, F.J. Gilbert, Use of new imaging techniques to predict tumour response to therapy, Lancet Oncol. 11 (1) (2010) 92–102.

[5] M. Banaie, H. Soltanian-Zadeh, H.R. Saligheh-Rad, M. Gity, Spatiotemporal features of dce-mri for breast cancer diagnosis, Comput. Methods Progr. Biomed. 155 (2018) 153–164.

[6] K. Vassiou, T. Kanavou, M. Vlychou, A. Poultsidi, E. Athanasiou, D.L. Arvanitis, et al., Characterization of breast lesions with ce-mr multimodal morphological and kinetic analysis: comparison with conventional mammography and high-resolution ultrasound, Eur. J. Radiol. 70 (1) (2009) 69–76.

[7] E.A. Hauth, C. Stockamp, S. Maderwald, A. Mühler, R. Kimmig, H. Jaeger, et al., Evaluation of the three-time-point method for diagnosis of breast lesions in contrast-enhanced mr mammography, Clin. Imag. 30 (3) (2006) 160–165.

[8] A.K. Heye, R.D. Culling, M.d.C.V. Hernández, M.J. Thrippleton, J.M. Wardlaw, Assessment of blood–brain barrier disruption using dynamic contrast-enhanced mri. a systematic review, Neuroimage Clin 6 (2014) 262–274.

[9] M. Leach, B. Morgan, P. Tofts, D. Buckley, W. Huang, M. Horsfield, et al., Imaging vascular function for early stage clinical trials using dynamic contrast-enhanced magnetic resonance imaging, Eur. Radiol. 22 (7) (2012) 1451–1464.

[10] J.Y. Kim, S.H. Kim, Y.J. Kim, B.J. Kang, Y.Y. An, A.W. Lee, et al., Enhancement parameters on dynamic contrast enhanced breast mri: do they correlate with prognostic factors and subtypes of breast cancers? Magn. Reson. Imaging 33 (1) (2015) 72–80.

[11] A. Karahaliou, K. Vassiou, N. Arikidis, S. Skiadopoulos, T. Kanavou, L. Costaridou, Assessing heterogeneity of lesion enhancement kinetics in dynamic contrast-enhanced mri for breast cancer diagnosis, Br. J. Radiol. 83 (988) (2010) 296–309.

[12] N.M. Braman, M. Etesami, P. Prasanna, C. Dubchuk, H. Gilmore, P. Tiwari, et al., Intratumoral and peritumoral radiomics for the pretreatment prediction of pathological complete response to neoadjuvant chemotherapy based on breast dce-mri, Breast Cancer Res. 19 (1) (2017) 57.

[13] W. Huang, A. Tudorica, S. Chui, K. Kemmer, A. Naik, M. Troxell, et al., Variations of Dynamic Contrast-Enhanced Magnetic Resonance Imaging in Evaluation of Breast Cancer Therapy Response: a Multicenter Data Analysis Challenge, (2014), https://doi.org/10.7937/k9/tcia.2014.a2n1ixox https://wiki.cancerimagingarchive.net/x/boEaAQ.

[14] K. Clark, B. Vendt, K. Smith, J. Freymann, J. Kirby, P. Koppel, et al., The cancer imaging archive (tcia): maintaining and operating a public information repository, J. Digit. Imag. 26 (6) (2013) 1045–1057.

[15] G. Sindhu Madhuri, Classification of image registration techniques and algorithms in digital image processing–a research survey, Int. J. Comput. Trends Technol. 15 (2014) 78–82.

[16] S.M.B. Netto, A.C. Silva, R.A. Nunes, M. Gattass, Voxel-based comparative analysis of lung lesions in ct for therapeutic purposes, Med. Biol. Eng. Comput. 55 (2) (2017) 295–314.

[17] G.z. ZHAO, Y.z. YANG, X.c. SONG, Modified otsu algorithm using quartered search method, DEStech Trans Mater Sci Eng (2016) 318–323 (mmme).

[18] B.K. Szabo, P. Aspelin, M.K. Wiberg, Neural network approach to the segmentation and classification of dynamic magnetic resonance images of the breast: comparison with empiric and quantitative kinetic parameters1, Acad. Radiol. 11 (12) (2004) 1344–1354.

[19] F. Baum, U. Fischer, R. Vosshenrich, E. Grabbe, Classification of hypervascularized lesions in ce mr imaging of the breast, Eur. Radiol. 12 (5) (2002) 1087–1092.

[20] U. Preim, S. Glaßer, B. Preim, F. Fischbach, J. Ricke, Computer-aided diagnosis in breast dce-mri–quantification of the heterogeneity of breast lesions, Eur. J. Radiol. 81 (7) (2012) 1532–1538.

[21] A.A. Taha, A. Hanbury, Metrics for evaluating 3d medical image segmentation: analysis, selection, and tool, BMC Med. Imaging 15 (1) (2015) 29.

[22] M.E. Celebi, H.A. Kingravi, P.A. Vela, A comparative study of efficient initialization methods for the k-means clustering algorithm, Expert Syst. Appl. 40 (1) (2013) 200–210.

[23] A.K. Jain, Data clustering: 50 years beyond k-means, Pattern Recogn. Lett. 31 (8) (2010) 651–666.

Otilio Paulo Silva Neto Received a degree in Information Systems from the Faculdade Integral Diferencial -Brazil in 2006. Master's at Electric Engineering from Universidade Federal do Maranho (2016). Currently he is a Professor at the Federal Institute of Piauí (IFPI), Brazil. He is aPhD student in electric engineering at Federal University of Maranhão. He works with image processing, especifically on medical imaging.

José Denes Lima Araújo Received a degree in Information Systems from the Federal University of Piauí - Brazil in 2015. Master's at Computer Science from Universidade Federal do Maranho (2018). Currently, he is PhD student in electric engineering at Federal University of Maranhão. He works with image processing, especifically on medical imaging.

Ana Gabriela Caldas Oliveira Received a medical degree from the Federal University of Maranhão (1996). Master's Degree in Oncology from the University of São Paulo (2005). PhD in Collective Health, Federal University of Maranhão (2017). She is currently Assistant Professor of Medicine at the Federal University of Maranhão. Higher Education Technique of the Municipal Health Department - São Luis (Ma). It works with general cancerology, breast cancer and female tumors, oncoplasty and epidemiology.

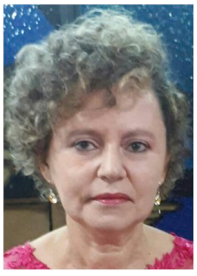

Mara Silvia Pinheiro Cutrim Currently a physician in the Radiology and Diagnostic Imaging Service of the University Hospital of the Federal University of Maranhão - HUUFMA. Coordinator of the Medical Residency Program in Radiology of the University Hospital of the Federal University of Maranhão - HUUFMA. Coordinator of the Radiology and Diagnostic Imaging Service of the Portuguese Hospital. He has experience in Medicine, with emphasis in Medical Radiology. She works with General Radiology, Ultrasound and Doppler, Computed Tomography and MRI in Internal Medicine, Gynecology and Obstetrics, Pediatrics, and in Mammary Radiology.

Aristófanes Corrêa Silva Received a PhD degree in Informatics from Pontifical Catholic University of Rio de Janeiro - Brazil in 2004. Currently he is a Professor at the Federal University of Maranhão (UFMA), Brazil. He teaches image processing, pattern recognition and programming language. His research interests include image processing, image understanding, medical image processing, machine vision, artificial intelligence, pattern recognition and, machine learning.

Anselmo Cardoso de Paiva Received BSc in civil engineering from Maranhão State Univeristy -Brazil in 1990, a MSc in civil engineering-Structures and a PhD in Informatics from Pontiphical Catholic University of Rio de Janeiro - Brazil in 1993 and 2002. Currently he is a Professor at theFederal University of Maranhão (UFMA), Brazil.

Marcelo Gattass Took his Ph.D. in 1982 from Cornell University and is a full professor at PUC-Rio. He currently teaches Computer Graphics and 3D Computer Vision for graduate students and Data Structures for undergraduates. He is also the Director of Tecgraf/PUC-Rio. Computer Graphics Technology Laboratory, where he supervises several industrycooperation projects in the areas of 3D modeling and visualization, geographic information systems, user interfaces, and web-based applications.